Ultrasonics Sonochemistry 74 (2021) 105558

Contents lists available at ScienceDirect

Ultrasonics Sonochemistry

journal homepage: www.elsevier.com/locate/ultson

Ultrasonication-assisted synthesis of 2D porous MoS_2/GO nanocomposite catalysts as high-performance hydrodesulfurization catalysts of vacuum gasoil: Experimental and DFT study

Zohal Safaei Mahmoudabadi [a,*], Alimorad Rashidi [b,*], Ahmad Tavasoli [a], Mehdi Esrafili [c], Mohammad Panahi [d], Mojtaba Askarieh [b], Saeed Khodabakhshi [e]

[a] School of Chemistry, College of Science, University of Tehran, Tehran, Iran
[b] Nanotechnology Research Center, Research Institute of Petroleum Industry, Tehran, Iran
[c] Department of Chemistry, University of Maragheh, Maragheh, Iran
[d] Elettra - Sincrotrone Trieste, S.S. 14 km 163.5 in AREA Science Park, Basovizza, I-34149 Trieste, Italy
[e] Energy Safety Research Institute, College of Engineering, Swansea University, Swansea SA1 8EN, UK

ARTICLE INFO

Keywords:
Hydrodesulfurization (HDS)
Vacuum gas oil
MoS_2
Graphene oxide
Nano composite catalyst

ABSTRACT

In this study, a novel, simple, high yield, and scalable method is proposed to synthesize highly porous MoS_2/graphene oxide (M−GO) nanocomposites by reacting the GO and co-exfoliation of bulky MoS_2 in the presence of polyvinyl pyrrolidone (PVP) under different condition of ultrasonication. Also, the effect of ultrasonic output power on the particle size distribution of metal cluster on the surface of nanocatalysts is studied. It is found that the use of the ultrasonication method can reduce the particle size and increase the specific surface area of M−GO nanocomposite catalysts which leads to HDS activity is increased. These nanocomposite catalysts are characterized by XRD, Raman spectroscopy, SEM, STEM, HR-TEM, AFM, XPS, ICP, BET surface, TPR and TPD techniques. The effects of physicochemical properties of the M−GO nanocomposites on the hydrodesulfurization (HDS) reactions of vacuum gas oil (VGO) has been also studied. Catalytic activities of MoS_2-GO nanocomposite are investigated by different operating conditions. M9-GO nanocatalyst with high surface area (324 m^2/g) and large pore size (110.3 Å), have the best catalytic performance (99.95%) compared with Co-Mo/γAl_2O_3 (97.91%). Density functional theory (DFT) calculations were also used to elucidate the HDS mechanism over the M−GO catalyst. It is found that the GO substrate can stabilize MoS_2 layers through weak van der Waals interactions between carbon atoms of the GO and S atoms of MoS_2. At both Mo- and S-edges, the direct desulfurization (DDS) is found as the main reaction pathway for the hydrodesulfurization of DBT molecules.

1. Introduction

In recent years, along with increasing the global concern on environmental protection, rigid environmental legislations have been made to restrict the sulfur content of fuels [1–7]. The hydrodesulfurization (HDS) is an effective industrial process to attain ultra-low-sulfur fuels [8–11]. Thus, future researchers should still focus on developing novel catalysts with a prominent performance in the HDS reaction. Generally, commercial HDS processes use transition metal sulfides such as molybdenum disulfide (MoS_2), usually supported on the Al_2O_3, Santa Barbara Amorphous-15 (SBA-15) or carbon materials [12–14]. The catalytic efficiency of MoS_2 based catalysts for hydrodesulfurization at low temperatures is still a challenge ahead because of poor dispersion and inadequate available active sites. By exfoliating the MoS_2, a thin-layer structure can be formed, for which an improved HDS activity is achieved through reducing the particle size, increasing the dispersion and amount of the active sites [8,15,16]. The relationship between the structure of the MoS_2 and the active sites in enhancing the catalytic performance is very valuable while many researches have been engaged in investigation about the activity and structure relationship [9,10]. A recent study [12,13] has shown a distinguished relationship between the HDS reaction and the number of Mo atoms in the corners and edges of MoS_2 crystallites. It should be noted that the better MoS_2 dispersions increases the catalytic activity in industrial catalysts [17–19]. Moreover,

* Corresponding authors.
E-mail address: rashidiam@ripi.ir (A. Rashidi).

https://doi.org/10.1016/j.ultsonch.2021.105558
Received 18 December 2020; Received in revised form 10 April 2021; Accepted 12 April 2021
Available online 22 April 2021

the selectivity of hydrogenolysis and hydrogenation reactions is correlated with the fraction of rim or edge sites. The fraction of edge sites has an impact on the selectivity of hydrogenolysis. A rim–edge model is proposed by Daage and Chianelli [20] in which it is supposed that the hydrogenation of the dibenzothiophene (DBT) to tetrahydrodibenzothiophene (THDBT) takes place individually on the rim sites although the hydrogenolysis of the DBT to biphenyl (BP) occurs on the edge planes of MoS_2 crystallites. Farag et al.[21] proposed a correlation between the selectivity in the HDS process and the average number of MoS_2 stacked layers. Generally, the HDS activity can be increased by some ways such as exfoliating the MoS_2 layers [19], decreasing the size of MoS_2 particles [22,23] and amending the dispersion of MoS_2 in composites [24]. There have also been a wide range of researches on the effects of support types on the HDS process [25,26]. Carbon structures such as carbon nanotubes (CNT), graphene (G), graphene oxide (GO) have been utilized as a promising support for many catalysts [27,28] including the catalysts used in HDS reaction [29]. The reported results showed that the GO-based supports due to surface functional groups such as carboxyl, carbonyl and hydroxyl groups form plenty of favorable nucleation sites for the adsorption of metal sulfides. This feature provides a better activity in the HDS process compared to the conventional alumina-supported catalysts [30]. Recently, nanocatalysts such as MoS_2/G [31,32], and MoS_2/GO [2] nanocomposites have been widely investigated due to synergistic interactions and combinations of physisorption, chemisorption and catalytic reaction. Besides, ultrasonication method has a wide application prospect in catalyst manufacturing [33–35]. The ultrasonic wave related to cavitation leads to a reduction in the occurrence of pore blockage and result in the incensement of the specific surface area and pore volume of catalysts [36,37].

Besides, quantum chemical calculations using the density functional theory (DFT) has been proven as an efficient tool to obtain useful information about the role of different factors in the mechanism of the HDS process over MoS_2 substrates [38,39]. For instance, by performing DFT calculations, Zheng et al.[40] showed the dependency of adsorption energies of H_2 and activation energies of the HDS on the various single S-vacancies in the basal plane of the MoS_2.

In the present work, M−GO nanocomposite catalysts have been prepared via the reaction of the graphene oxide and co-exfoliation of commercial MoS_2 in the presence of polyvinyl pyrrolidone (PVP) under ultrasonication. In addition, the effects of physicochemical properties in enhancing the catalytic efficiency of the M−GO nanocomposites in the HDS reactions of VGO have been thoroughly investigated. The effect of parameters such as pressure, temperature, LHSV, and ratio of hydrogen/feedstock on the HDS reaction of the VGO by using the M−GO nanocomposites as catalyst have been perused. Among the obtained catalysts, the M9-GO nanocomposite catalyst showed an efficient HDS activity on the VGO feedstock, particularly at facile operation conditions such as a low temperature, pressure, H_2/Feed (VGO) ration and a high LHSV). Moreover, to shed light on the HDS mechanism on the M−Go nanocomposites, first-principles density functional theory (DFT) calculations were performed. To this aim, a proper molecular model of the M−GO was constructed and the adsorption properties of H_2 and DBT molecules were explored. According to the DFT calculations, it was found that the HDS process is considerably dependent on the sulfur coverage on the Mo-edge of the catalyst.

2. Experimental section

2.1. Materials

In this research, molybdenum disulfide powder (greater than99%, particle size < 5 μm), Polyvinylpyrrolidone (PVP) (MW $\sim$ 10000) and graphite ($\geq$99%, particle size < 45 μm) were obtained from Sigma-Aldrich and other chemicals materials were used as analytical grade without any further purification. The chemical composition of the prepared GO was; C: 56.20 wt%, O: 40.32 wt%, H: 2.88 wt%, N: 0.2 wt% and S: 0.4 wt%.

2.2. Synthesis of catalysts

A series of 2D porous MoS_2/GO nanocomposite catalysts were prepared through the PVP-assisted ultrasonication method. In this synthesis procedure, a suspension of the MoS_2 nanoflakes was prepared by adding MoS_2 powder to ethanol followed by addition of the PVP under 30 min ultrasonication at the temperature of 15 ^{0}C to achieve a homogeneous dispersion. The obtained suspension had a high stability at ambient conditions. Then, the GO was prepared through the Hammers' method [41,42]. The specific volumes of the GO solution were prepared with given concentration, added to a solution containing exfoliated MoS_2 and mixed for 20 min. The resulting suspension was transferred into a breaker and then probe-sonicated for 15 min at 40 Hz. After that, the product was collected by centrifugation with the rate of 6000 rpm for 30 min and was washed with deionized water/ ethanol several times and then was dried in the vacuum oven at 60 °C for a period of at least 24 h. Considering the amount of the Mo in the solutions, the PVP content was changed (PVP /Mo = 5 wt%). Also, ultrasound with 20, 40, 80 and 100 W output powers was applied in the synthesis process of the M−GO nanocomposite catalysts.

2.3. Catalyst characterization

The powder X-ray diffraction (XRD) patterns were collected on a diffractometer (Philips, PW1730) with Cu Kα radiation ($\lambda = 1.54178$ Å). Textural properties were determined by a physisorption analyzer (Micromeritics, ASAP 2010). The specific surface areas and pore size distribution were measured using the Brunauer-Emmett-Teller (BET) method and the Barrett-Joyner-Halenda (BJH) method, respectively. Raman spectra were obtained using a micro-Raman spectrometer (Thermo Fisher Scientific, DXR), equipped with a CCD camera detector with 532 nm excitation. The UV/Vis absorption spectra were acquired by a spectrometer (Shimadzu, UV-2550) at room temperature. Photoluminescence data (PL) were carried out using a spectrophotometer (Horiba, FluoroMax-4) at room temperature. The acidity of the prepared nanocatalysts was determined via employing the temperature programmed desorption of ammonia (NH_3-TPD) in a quartz micro reactor (Quantachrome, ChemBET-3000).The reductive property of the nanocatalysts was measured by means of the temperature-programmed reduction (H_2-TPR)using a chemisorption analyzer (Micromeritics , Autochem II-2920). Scanning Electron Microscopy (SEM) images were taken to determine the morphologies by a scanning electron microscope (ZEISS, Sigma). High-resolution transmission electron microscopy (HR-TEM) and scanning transmission electron microscopy (STEM) images were captured on a microscope under 200 kV acceleration voltage (Philips , CM200/FEG). The topography of the nanocatalysts were achieved using an atomic force microscope (AFM, NT-MDT, SOLVER). The X-ray photoelectronic spectroscopy (XPS) on the nanocatalysts were carry out by an AXIS ULTRA-DLD spectrometer using a 1487 eV, Al Kα photon source. The peak-fitting of XPS spectra were performed using CASAXPS program. A Shirley-type background and a line shape convoluted with a Gaussian-Lorentzian profile were applied in all spectra to decompose them into the spectral components. The Mo concentrations of the nanocatalysts were clarified through exploiting the inductively coupled plasma-optical emission spectrometry (Perkin Elmer, ICP–OES.). To determine the sulfur content of the liquids after the HDS process, energy dispersive X-ray fluorescence (EDXRF) method was employed by means of an X-ray sulfur meter (Tanaka, RX-360SH). Also, gas chromatography with an atomic emission detector (Hewlett Packard HP-5890A) was used to measure the distribution of sulfur or carbon atoms in the fuel.

2.4. Catalytic experiments

Catalytic activities were evaluated in the HDS on the VGO at the different operation conditions (temperature, pressure, LHSV, and the ratio of H_2/Oil) in a high-pressure continuous fixed-bed stainless steel reactor (length:700 mm and diameter:20.6 mm). The nanocatalysts with carborundum filler (20–30 mesh particle size) were mixed and used to perform the HDS process. The characteristics of the feed and schematic of the reactor setup are presented in the supplementary information. The catalytic activity of nanocatalysts was measured at steady-state conditions, after at least 24 h on-stream. Finally, the feed and reaction products were collected and analyzed by a total sulfur analyzer according to the ASTM 5453 standard. Eq. (1) is described in detail in the supplementary material which was used to determine the catalytic conversion.

$$HDS(\%) = ((S_o - S_s)/S_o)*100 \quad (1)$$

2.5. Computational details

In this study, the spin-polarized DFT calculations were performed using the DMol3 package [43]. The exchange–correlation energy was approximated by Perdew, Burke and Ernzerhof (PBE) density functional [44]. To account weak dispersion energies, the Grimme scheme was adopted [45]. The wave functions of all atoms were described by a double numerical plus polarization (DNP) basis set. To consider the relativistic effects of the Mo atoms, the DFT semicore pseudopotential (DSPP) method was implemented [46]. For the self-consistent field (SCF) calculations, a convergence tolerance of 10^{-6} Ha was adopted.

To model the primitive graphene, a supercell including 130 carbon atoms was employed. To avoid dangling bonds, the edge carbon atoms were passivated by addition of hydrogen atoms. Despite many possible models for the GO, we adopted a simple model for this substrate as hexagonal carbon network with both sp^2 and sp^3 hybridized carbon atoms with an epoxy group on its "basal" plane. The MoS_2/GO nanocomposite was obtained by decoration of a 4 × 4 cluster of MoS_2 on the GO. The adsorption energy $E_{ads}(X)$ of the different species over the MoS_2/GO was evaluated by the following equation:

$$E_{ads}(X) = E_{XS} - -(E_X + E_S) \quad (2)$$

In which E_{XS} represents the total energy of X species adsorbed on the MoS_2/GO, while E_X and E_S denote the energy of isolated X and the MoS_2/GO, respectively.

All the transitions states were located using the linear synchronous transit)/quadratic synchronous transit (LST/QST) method [47]. Following the reaction path from the reactant to the product, the LST/QST approach searches a single interpolation to a maximum energy in order to obtain the transition state. The nature of located transition states was then checked by the frequency analysis, in which one and only one negative frequency was obtained for each transition state in the direction of reaction path. To find the intermediate structure, the minimum energy path of each reaction was carefully analyzed.

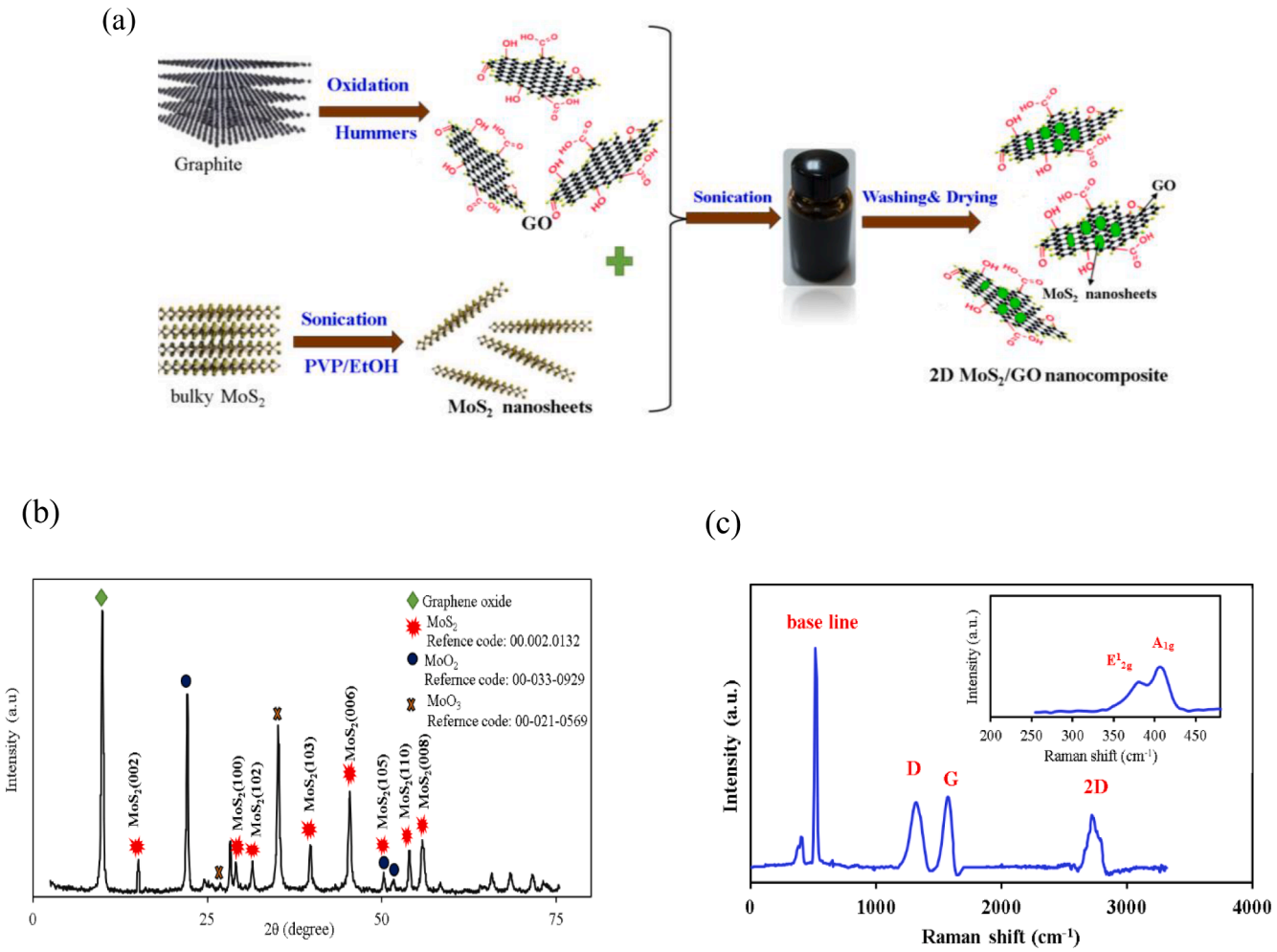

Fig. 1. (a) The schematic illustration of the preparation of the MoS_2-GO (b) XRD pattern of the M9-GO (c) Raman spectra of the M9-GO.

3. Results and discussion

3.1. Catalyst characterizations

Facile synthesis of the 2D porous MoS_2/GO nano composite catalysts via PVP is described in Fig. 1a. The PVP is a water-soluble polymer that can be also dissolved in large amounts of organic solvents such as ethanol and isopropanol. The 2D structure of the PVP which is composed of hydrophobic methylene and hydrophilic amide groups plays a significant role in exfoliation and intercalation of MoS_2 from bulk to 2D [48,49]. The ultrasonic process leads to the phenomenon of cavitation which is useful to improve the activity and stability of the nanocomposite catalysts. In fact, the effect of ultrasonic waves on the preparation of M−GO nanocomposite catalysts can decrease the occurrence of pore blockage, thus the specific surface area, the pore volume of catalyst, and the total acid content noticeably increased. Also, the M−GO nanocomposite catalysts were synthesized by the ultrasonic method, the particle size of MoS_2 decreased and the active metal is uniformly dispersed on GO. The changes in the particle size distribution of MoS_2 after ultrasound treatment are demonstrated in Table S2. The results displayed that ultrasound treatment had a remarkable effect on the particle size distribution of MoS_2. The cavitation phenomenon that results in turbulence, leads to the breakdown of MoS_2 particles. As a result, the decrease in particle size can be related to the turbulence and cavitation forces of the ultrasound treatment. The most appropriate average particle size of MoS_2 belonged to the ultrasound treatment for 30 min at 80 W in which the more effective active site can be exposed to the HDS reaction and the catalyst activity was higher. Then, by adding the GO layers to the obtained solution, MoS_2 flakes were distributed homogenously over the GO layers. The Mo loading, specific surface area and pore volume of the GO and 2D MoS_2/GO nanocomposite catalysts are shown in Table1.

The M9-GO nanocomposite with the Mo loading of 9 wt% was characterized by XRD as illustrated in Fig. 1b. The characteristic peak emerged at $2\theta = 10.6^\circ$ corresponds to an interlayer distance of 0.8 nm is assigned to the GO [50]. The number of layers and stacking height were determined as 12, and 9.104 nm respectively by applying Debye-Scherrer equation for the M9-GO. It should be noticed that the d-spacing of the graphite was ~ 0.34 nm while it was ~ 0.87 for that of the GO. This increase possibly depends on the formation of functional groups which possess oxygen; e.g., hydroxyl, epoxy, and carboxyl groups over the GO surface [51]. Fig. 1b demonstrates the XRD patterns of the synthesized material compared with the MoS_2, MoO_2, and MoO_3 as reference The peaks at $2\theta = 14.5^\circ$, 30.4°, 31.5°, 39.5°, 45.0°, 50.03°, 58.5°,60.5° and $2\theta = 26.5^\circ$, 35.0° can be attributed to the MoO_2 (JCPDS 00–033-0929) and MoO_3 (JCPDS 00–021-0569) respectively [52]. The peaks at $2\theta = 23.5^\circ$, 50.0°, 53.1° are coincided to the hexagonal MoS_2 phase (JCPDS 00–002-0132) [37], The recognized peaks of the MoO_2 and MoO_3 phases are related to the oxidation states of the Mo species that can be attributed to the process of chemical exfoliation conducted by the ultrasonication method in this study. After the chemical exfoliation in the ultrasonication process using the PVP, the synthesized MoS_2 displays lower peak intensity showing the decrease in crystallinity. A little shift of the (0 0 2) peak to the left and its downshift and broadening peak can also be originated from the increase in the interlayer distance and the size shrinkage in the c-axis direction, respectively. Thus, the results from the XRD patterns implied that the interlayer spacing of the MoS_2 nanostructure was expanded after performing the exfoliation process through a chemical reaction and accordingly the thickness of MoS_2 sheets was reduced. For a better comparison, the XRD spectrum of bulky MoS_2, MoS_2 nanosheets, MoO_2, and the pristine GO are presented in Fig. S2. The Raman spectrum of the M9-GO nanocomposite catalyst is represented in the Fig. 1c. The peaks at 385 and 410 nm are attributed to E^1_{2g} and off-plane A^1_g vibrations of the MoS_2 hexagon crystal [53]. In addition, the peaks at 1340 nm (I_D) is related to the D bond which represents the defects of the GO structure, 1600 nm(I_G) is associated to the G bond which shows the graphite structure of the GO and 2600 nm (2D) associated to the 2D bond which is a G-complementary structure of the GO, respectively. In fact, higher values of I_D/I_G demonstrate more structural defects and functional groups in the GO structure and higher values of the I_{2D}/I_G represent formation of fewer layers or sheets in the GO structure, accordingly, the synthesized GO was composed of 2–3 layers [54]. As it can be seen, the G band of the GO for the M9-GO nanocomposite is up-shifted to 1600 cm^{-1}. An electronic interaction between the MoS_2 nanostructure and GO sheets may be the possible reason for this shift, cause of a dyadic bonding between the surface of GO and MoS_2 nanosheets. Table 1 represents the classified values of the Mo loadings, specific surface areas, pore volumes, average pore diameter and acidity of the synthesized catalysts. The results acquired from the BET method clarified that the surface area of the nanocatalyst samples followed a decreasing trend with loading active metals on the GO. Furthermore, the surface area of the synthesized graphene oxide was 355 m^2/ g while all other synthesized nanocomposites proportionally showed lower surface areas with Mo content. In addition, the TPD results demonstrated that the nanocomposite acidities were increased upon loading the active Mo onto the GO.

Table 1
Characteristic and pore structure parameter of synthesized nanocatalysts with the various Mo loading.

Catalyst	Mo loading (wt. %)	Surface area* (m^2/g)	Pore volume (cm^3/g)	Average pore diameter (nm)	Acidity mmol NH_3/g
GO	0	355	1.05	14.03	–
M5-GO	5	332	1.1	13.50	1.1
M 9-GO	9	324	1.05	11.03	1.7
M13-GO	13	315	1.30	9.23	1.8
M17-GO	17	309	1.10	7.60	1.7
M20-GO	20	260	1.15	6.40	1.6

In Fig. 2, the M9-GO nanocomposite has been investigated through the XPS technique. The presence of carbon, oxygen, sulfur, molybdenum, and negligible amount of impurities are demonstrated in the survey spectrum (Fig. 2a). As shown in Fig. 2b, the dominant peak at 284.0 eV in C 1 s spectrum, is corresponding to the sp^2 hybridized C–C bonds in the GO. There are four peaks located at 282.4, 284.0, 284.5, and 287.7 eV corresponding to the GO-MoS_2 interaction (6.80%), C–C (89.70%), C = O (2.53%) and O-C = O (0.97%) functionalities, respectively. No notable feature was observed in the O1s spectra showing the formation of a chemical bond between the oxygen side of the GO and the MoS_2 nanostructure (Fig. 2c). In addition, the Mo $3d_{5/2}$ (at 229.1 eV) and $3d_{3/2}$ (at 232.1 eV) doublets are in line with Mo^{4+} (Fig. 2d), while the S $2p_{3/2}$ (at 161.9 eV) and $2p_{1/2}$ (at 163.2 eV) doublets related to the S^{2-} (Fig. 3e), which are in a good agreement with the standard XPS data of the MoS_2. Additionally, XPS spectra indicated that the Mo/S ratio is close to 0.5, as the stoichiometric MoS_2 on the surface of the GO. Several shoulders and peaks in Mo 3d, S 2p and C1s spectra are evidence of a strong interaction between carbon atoms in the GO and the MoS_2 nanostructure. However, it is a sophisticated task to assign those peaks individually. . It should be stated that the stoichiometry value is associated with an error of<5% according to the limitation of the instrumentation and the processes of fitting.

The results attest to the success in the synthesis of the M9-GO as confirmed by SEM micrographs. The elemental distribution of M9-GO composites is displayed in Fig. 3, where, all of C, O, S, and Mo elements were homogenously distributed over the GO surface. In Fig. 3, (b-e) the SEM-EDS mapping of the M9-GO indicates that the Mo/S ratio (1.03/2.05) is near to the MoS_2 stoichiometry which is in accordance with the XPS data. As it can be observed, the MoS_2 nanosheets on the GO nanocomposites have been successfully prepared using the

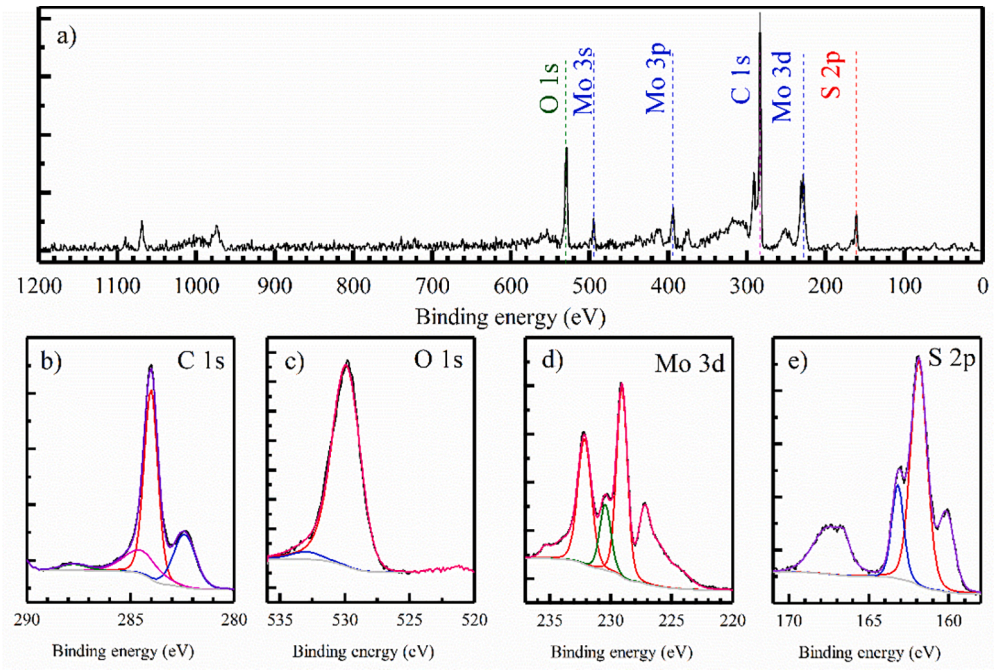

Fig.2. XPS spectra of the M 9-GO nanocomposite, a) the survey spectrum, b-e) C 1 s, O 1 s, Mo3d and S2p spectra, respectively.

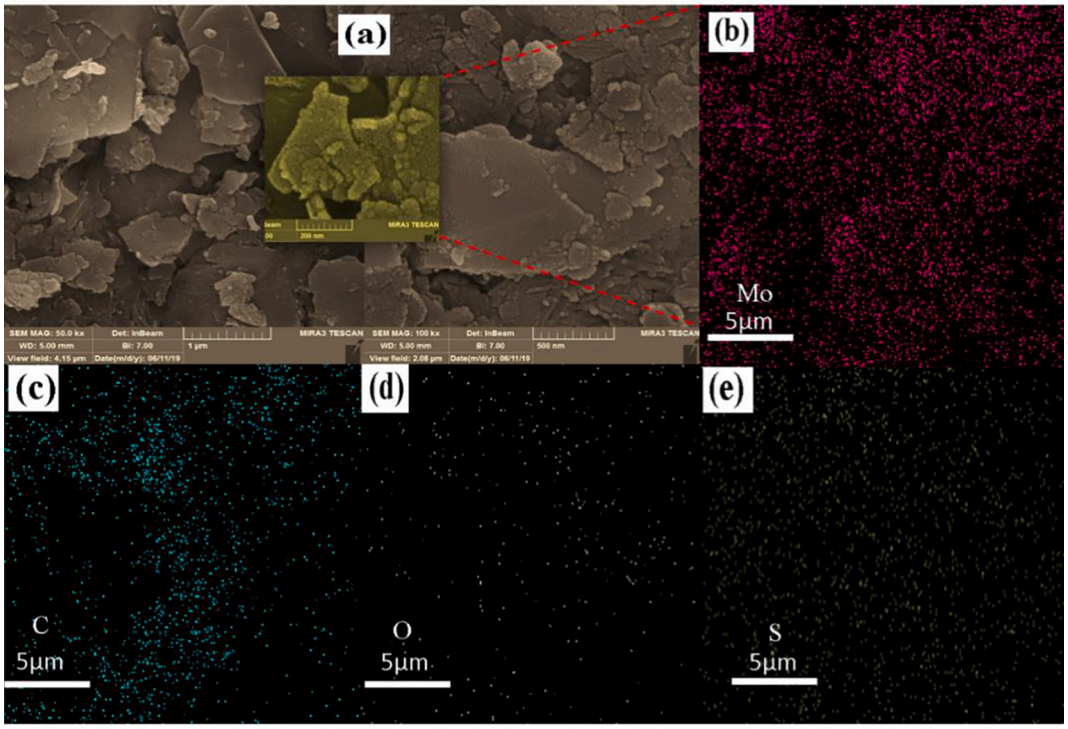

Fig. 3. SEM images of (a) the M9-GO nanocatalyst and (b)-(e) SEM-EDX element mapping of the M9-GO nanocatalyst.

ultrasonicated-assisted method. The GO monolayers produced through chemical exfoliation of graphite by using the Hummer's method [55] not only provided a relatively large area for the MoS_2 deposition, but also prevented the MoS_2 flakes restacking by their effective functional groups during the synthesis process. This employed nanocomposite structure offers an outstanding promotional influence on the HDS catalyst activity [56].

In Fig. 4, the morphology of GO and M9-GO was studied by atomic force microscopy (AFM), respectively. We have used the contact mode AFM to distinguish the thickness variation and to measure the surface topography of the GO and the M9-GO nanocomposite. Fig. 4a and 4b show three-dimensional and two-dimensional images of GO surfaces. The wrinkle sheets and their overlaps are distinctly detectable in the image. The thickness of the sheets was about 0.8 nm which relates to the monolayer GO sheets [57,58]. In addition, the uniform dispersion of MoS_2 nanoparticles on the surface of the GO observed in 3D and 2D images of the M9-GO nanocomposite (Fig. 4c, 4d) leads to an increased catalytic activity in the HDS process. Normally, the average thickness of

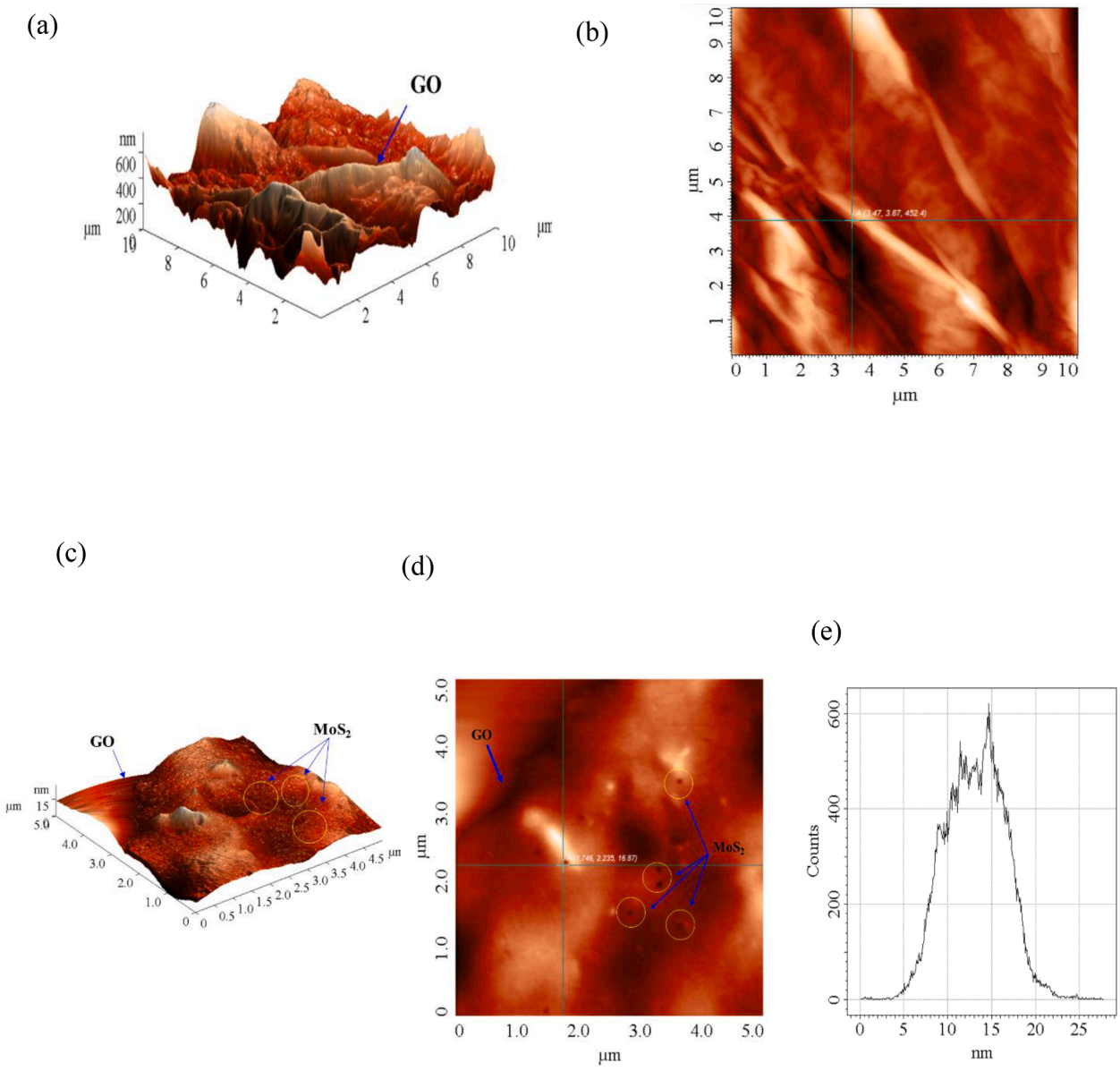

Fig. 4. (a) 3D AFM images of the GO,(b) 2D AFM images of the GO, (c) 3D AFM images of the M9-GO nanocatalyst,(d) 2D AFM images of the M9-GO and (e) size distribution of the M9-GO nanoparticle.

the M9-GO nanocomposite obtained from the line of the profile was about 15 nm (Fig. 4e).

The nanosheet-like morphologies of the GO and the M9-GO composite are further confirmed by STEM, TEM, and HR-TEM images. The STEM images of the M9-GO nanocomposite indicate that the MoS_2 nanoparticles as the active sites were distributed homogeneously on the GO surface (Fig. 5a and 5b). Furthermore, the few thin GO layers (Fig. 5c) and homogeneously distributed MoS_2 particles with the size of less than about 10 nm, conform the successful formation of the MoS_2 nanoparticles homogeneously on the GO layers (Fig. 5d). As it can be observed from Fig. 5e and 5f, the MoS_2 in the M9-GO nanocomposite had a well-layered structure with a measured d (0 0 2) of 0.64 nm, which is in line with the results obtained from the 2H crystal structure of MoS_2 and the XRD patterns. In addition, the number of MoS_2 layers is not exceeding 4–5 layers, which indicates few-layer structure of MoS_2 in the M9-GO nanocomposite. The MoS_2 particles can be grown selectively atop the GO which is alluded to the presence of oxygenated functional groups of the GO and their interactions with the Mo precursor [59]. The GO layers acted as the center for the MoS_2 nucleation and growth to form few-layer structures. It is thought that the crystal growth is hindered by the presence of functional groups which prevent the serious stacking of MoS_2 nanosheets. Thus, the as-formed monolayer MoS_2 nanosheets and GO nanolayers contributed to an increase in the cross-overlap-covered structure. Generally, the nanocomposite catalysts can provide an excellent activity in the HDS process, which is originated from the size of the metal particles being within a nanoscale range and also the homogenous distribution of the metal active phases over the GO surface [57]. Thus, the as-prepared M9-GO nanocomposite with a favorable MoS_2 nanoparticle dispersibility on GO sheets may have a proper prospect for hydrodesulfurization.

The NH_3-TPD and H_2-TPR techniques were employed as a simple method to investigate the catalytic properties of the M9-GO nanocomposite. According to the NH_3-TPD profile (Fig. 6a), the M9-GO nanocomposite showed two peaks at high temperatures, over 500 °C, which is associated with acid sites with strong acidity [8]. Many studies illustrate that the catalysts with stronger acid sites lead to a higher hydrogenation activity and so to the higher conversion [60].Thus, catalysts with strong acid sites like the M9-GO nanocomposite in this study was

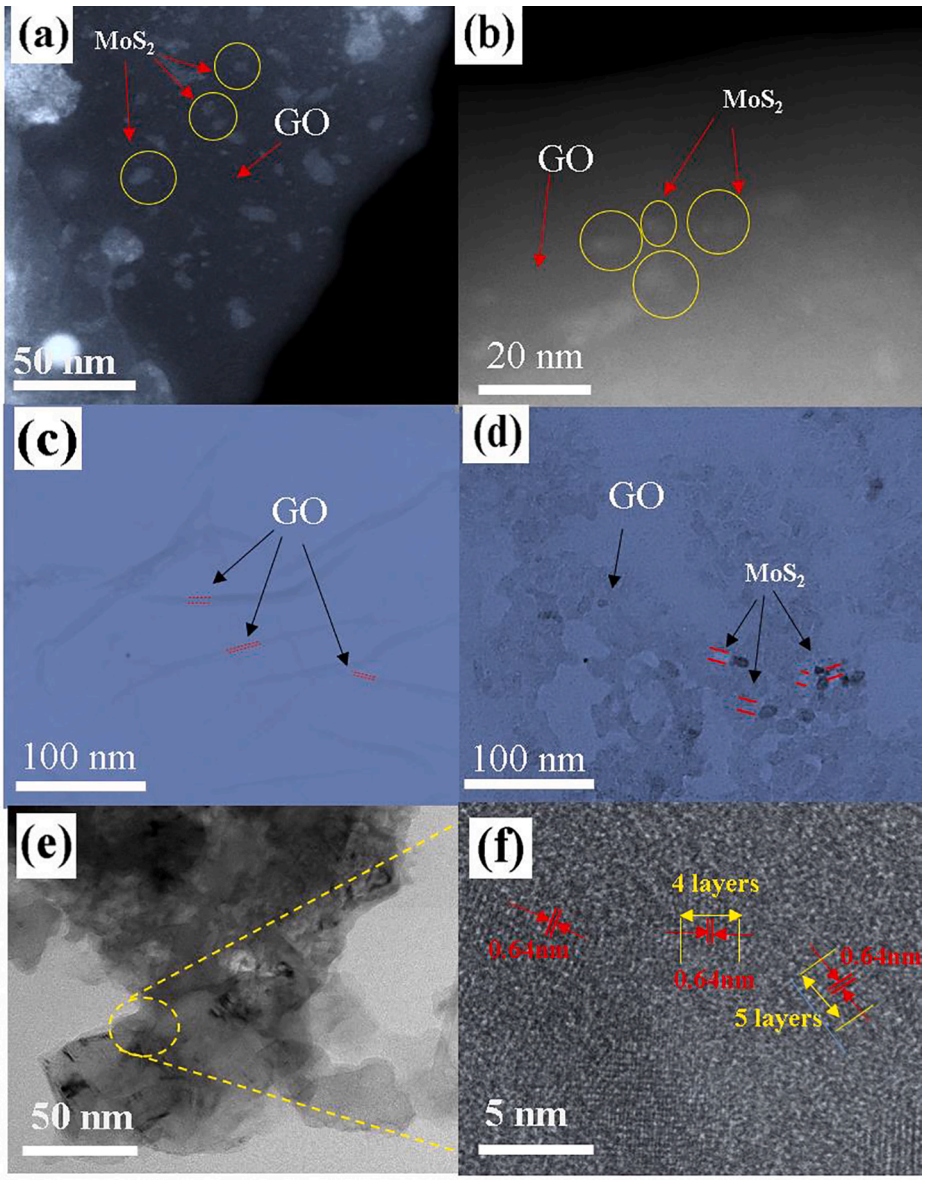

Fig.5. STEM images of (a, b) the M9-GO nanocatalyst, TEM images of (c) GO, (d) the M9-GO nanocatalyst and HR-TEM images of (e, f) the M9-GO nanocatalyst.

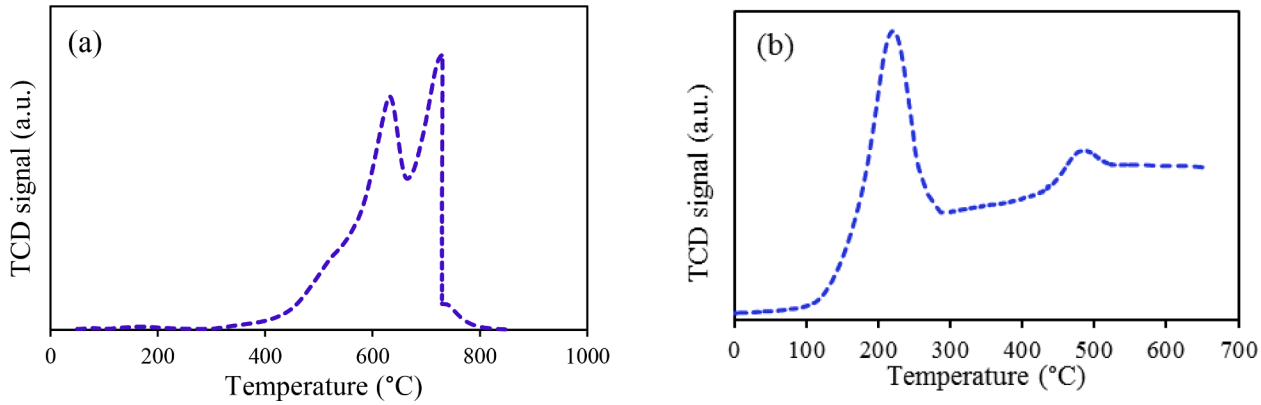

Fig. 6. (a) NH_3-TPD profile of the M9-GO nanohybrids catalyst (b) The TPR profiles of M9-GO nanohybrids catalyst calcined at 700 °C.

expected to show high catalytic activity for the HDS reaction because of the high adsorption between sulfur compounds and the acid sites [56]. The resulting H_2-TPR profile (Fig. 6b) exhibits two distinct peaks in the temperature range of 160 to 556 °C for the M9-GO nanocomposite. The first reduction peak (150–300 °C) corresponds to the reduction of S_2^{2-} groups on MoS_2 and excess-sulfur [61]. By the homolytic hydrogen separation, the interaction between S_2^{2-} groups and hydrogen is identified to generate equilibrium amounts of –SH groups [62]. Therefore, the effective excess-sulfur species in the M9-GO nanocomposite catalyst represented their impact on the hydrogenating properties. The second reduction peak (436–550 °C) is assigned to the partial reduction of Mo octahedral polymeric species from Mo^{6+} to Mo^{4+}[62].

3.2. Catalytic activity in the hydrotreating process

The VGO typically contains various sulfur compounds including linear structure such as mercaptans, sulfides (about 15%) and ring structure (e.g. thiophene and condensed-ring thiophenes) which constitute the main portion (about 85%) of the sulfur compounds [63,64]. It should be noted that DBTs are the major condensed-ring structure of sulfur components in the VGO feed [65]. Therefore, two routes of DBT hydrodesulfurization have been suggested: One is the hydrogenolysis (DDS) route where the sulfur atom is directly removed without hydrogenation of the aromatic ring structure, while the other is the hydrogenation (HYD) route where the hydrogenation of an aromatic

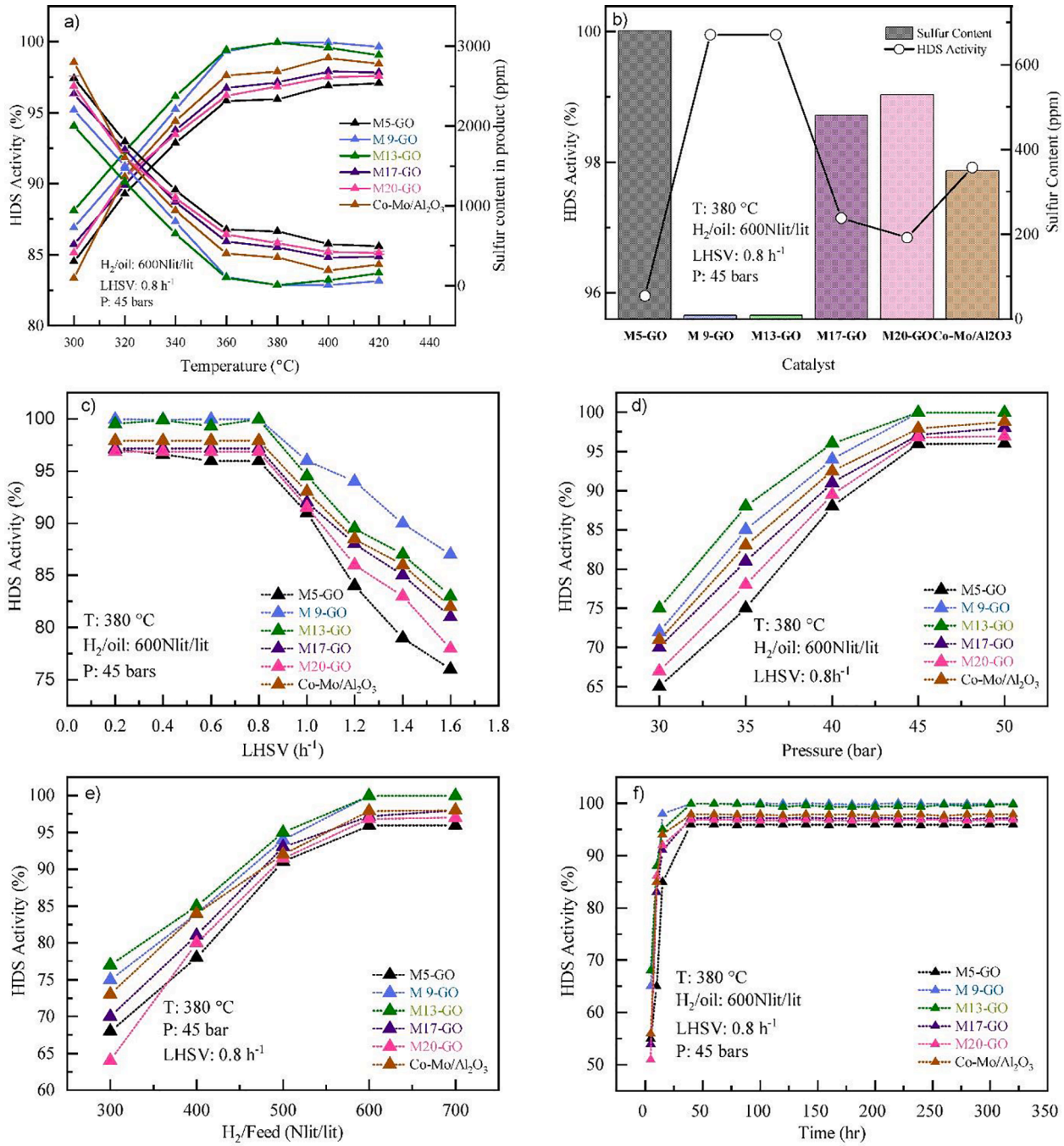

Fig. 7. The HDS conversion of the VGO a) Various MoS_2-GO nanocomposites in compare to the Co-Mo/γAl_2O_3 at T = 300–420 °C, b) at T = 380 °C, c) at LHSV = 0.2–1.6 h^{-1} d) at P = 30–50 bars, e) at H_2/oil ratio = 300-700NL L^{-1}f) long-term HDS conversion study of various MoS_2-GO nanocomposites and Co-Mo/γAl_2O_3 over a period of 320 h.

ring occurs prior to the hydrogenolysis of the C-S bond and the DBT is converted to the hexahydro dibenzothiophene (HHDBT) and/or tetrahydro dibenzothiophene (THDBT) followed by the formation of cyclohexylbenzene (CHB) and bicyclohexyl (BCH) (Fig. S4) [8,66]. Table S3 demonstrated the selectivity achieved at 40% of DBT conversion and HYD/DDS ratios for the different Mo-GO nanocatalysts. Regardless of the MoS_2-loading, the reaction products were: biphenyl (BP) as main product, along with the THDBT, CHB, and BCH. This is in good agreement with previous reports on the MoS_2 catalysts [67–69]. Based on the selectivity data, this is the main reaction product for all investigated catalysts. To acquire information about the role of MoS_2 in the preferential route of the HDS reaction, the HYD/DDS ratio was measured considering the selectivity data collected in Table S3. The HYD/DDS ratio showed the following trend: M9-GO > M13-GO > Co-Mo/γAl_2O_3 > M17-GO > M20-GO > M5-GO. This behavior could be correlated with the structure and morphology of the synthesized M−GO nanocatalysts since a similar tendency is displayed by the slab stacking and length of MoS2 layers [56,70,71]. Also, an enhancement of the HDS reaction and hydrogenation activities can be associated with an increase in the dispersion of the active phase [56,71]. It has been already proven that the HDS reaction of the DBT in the presence of the MoS_2 based HDS catalysts leads to the occurrence in the DDS pathway. In fact, the active catalytic centers are placed on the defects and the edges of the MoS_2 layered stacks [72]. Also, the M9-GO nanocomposite catalyst commonly selected the DDS pathway in HDS of the DBT, which was related to the decrease in the size, development of the porous structure of the MoS_2 and homogeneous distribution of the MoS_2 particles as the active islands on the surface of the GO resulting in a high performance in the HDS process. In addition, the turnover frequency (TOF) was calculated using the data obtained through H_2-chemisorption analysis (detailed description is available in supplementary data, Table S1) to explain catalytic activity which related to the number of exposed active sites on the catalyst [73,74]. According to the other results presented in Table S4., it is clearly observed that the M9-GO catalyst with 9 wt% Mo metal led to an increase in the activity of individual active catalytic sites in comparison with other catalysts in the HDS reaction.

3.2.1. Effect of operation condition

Some experiments were performed to compare the HDS performance on the VGO by various MoS_2-GO nanocomposites along with the commercial Co-Mo/γAl_2O_3 catalyst with similar loading of Mo at different operating temperatures, pressures, LHSVs and the ratios of hydrogen/feedstock. The influence of each parameter on the HDS performance was investigated while all other parameters stayed constant at default values. The results are shown in Fig. 7.For all samples; the experimental error was within 3%–5%.

The effect of the operating temperature on the HDS conversion of the VGO was studied through a temperature range of 300 to 420 °C under typical industrial conditions of 45 bars, 0.8 h^{-1} LHSV and hydrogen to feed ratio of 600 Nlit/lit. In Fig. 7a, it can be seen that the HDS conversion rates for all samples were enhanced with increasing of the temperature. It can be explained by the fact that at higher temperatures the heteroatoms were eliminated with higher rates while at elevated temperatures, the cracking of the reactants and increasing in the coking formation rate resulted in deactivation of the catalyst [75]. Also, in Fig. 7a, comparison of the synthesized nanocomposite catalysts and commercial Co-Mo/γAl_2O_3 catalyst is presented. The experimental results showed that the maximum HDS conversion efficiency for the VGO was obtained for the M9-GO catalyst at 380 °C while that for Co-Mo/γAl_2O_3 catalyst was at 420 °C, which indicated better performance of the M9-GO catalyst. The week dispersion and serious agglomeration of the MoS_2 nanostructure which is typically expected at high temperatures can be likely the cause of the observed decrease in the HDS efficiency. The residual sulfur content after HDS reaction over M9-GO, and Co-Mo/γAl_2O_3 catalyst were about 8, and 350 ppm at 380 °C, respectively which it is a considerable performance improvement (Fig. 7b). At the reaction temperature of 380 °C, the catalytic performance showed the following trend : M9-GO ~ M13-GO≫Co-Mo/γAl_2O_3 > M17-GO > M20-GO > M5-GO.

Fig. 7c presents the comparison of the various MoS_2-GO nanocomposites and Co-Mo/γAl_2O_3 (commercial) catalysts with varied LHSV (0.2–1.6 h^{-1}), where an increase in the LHSV could decrease the HDS conversion. The most suitable LSHV for the M9-GO and Co-Mo/γAl_2O_3 catalyst was obtained to be 0.8 h^{-1}.

In Fig. 7d, the influence of pressure (30, 35, 40, 45, 50 bar) on the HDS conversion is investigated. The results show that the M9-GO catalyst at the pressure of about 45 bar, temperature of 380 °C and LHSV of 0.8 h^{-1} reaches the maximum HDS conversion efficiency, while the Co-Mo/γAl_2O_3 catalyst showed low conversion efficiency even at the maximum operating pressure (50 bar). Therefore, for certain conversion efficiency, the required operating conditions for the M9-GO catalyst were favorable. This is due to the fact that the good dispersion of MoS_2 nanoparticles on the surface of the GO resulted in a lower required pressure for hydrogen penetration for the adsorption and surface reactions.

In Fig. 7e, it is observed that with the increase in the hydrogen to oil ratio, the HDS conversion is enhanced significantly. The most suitable ratio for the M9-GO and Co-Mo/γAl_2O_3 catalyst was obtained at 600 and 700 Nlit/lit, respectively. As observed, the hydrogen consumption of the M9-GO catalyst was less, which is economically very important.

Fig. 7f illustrates the HDS conversion as a function of time at the optimal operating conditions for the M9-GO. As it is demonstrated, the M9-GO catalyst can acceptably retain its sustainability for more than 320 h.

The higher catalytic activity of the unsupported M9-GO catalyst compared to the supported commercial catalyst used in this study is noticeable. This higher activity can be attributed to the provided strong acid sites. In addition, the decrease in the lateral size and an increase in the porosity and surface area with a good dispersion of the MoS_2 nanoparticles over the GO could provide more active sites in the HDS reaction leading to a high performance in desulfurization.

3.2.2. Effect of surface area and acidity on HDS reaction

As shown Fig. 8a, among the various synthesized nanocomposites, the surface area of the M9-GO, and M13-GO nanocomposites were determined as 324 and 315 m^2g^{-1}, respectively. This resulted in increasing the dispersion of MoS_2 nanoparticles on the surface of GO, and the stabilization of metals through weak interaction with the support in which subsequently increases the active sites for the HDS. Moreover, the pore size of M9-GO and M13-GO nanocomposites was 11.03, and 9.23 nm, where, the pores with larger sizes can facilitate the interaction among the trapped sulfur compounds and accordingly the pore-blockage is reduced (deactivation) by forming cokes or deposition of metals during a reaction. The acidity of the M9-GO and M13-GO nanocomposite catalysts was 1.7, and 1.8 $mmol.g^{-1}$ respectively which led to an increased efficiency in the HDS process (Fig. 8b).

3.3. DFT results

For a deeper understanding of the catalytic mechanism of the catalysts used in the HDS process, detailed DFT calculations were carried out on some appropriate molecular models. As seen in Fig. 9(a-b), the GO substrate was modeled by a large carbon cluster functionalized by an epoxy functional group at the center of the cluster. Due to the addition of the epoxy group, hybridization of those carbon atoms attached to the O atom changes from sp^2 to sp^3. Consequently, these carbon atoms show a large surface activity toward the MoS_2 cluster decorated on the GO owning to van der Waals interactions between the π electron density of the GO and lone pairs of S atoms. According to the previous studies [76–78], the HDS activity of MoS_2 depends significantly on the number of vacancies and sulfur coverage present at its edge. By performing DFT calculations, Sharifvaghefi et al. [67] have proven that H_2 molecules can

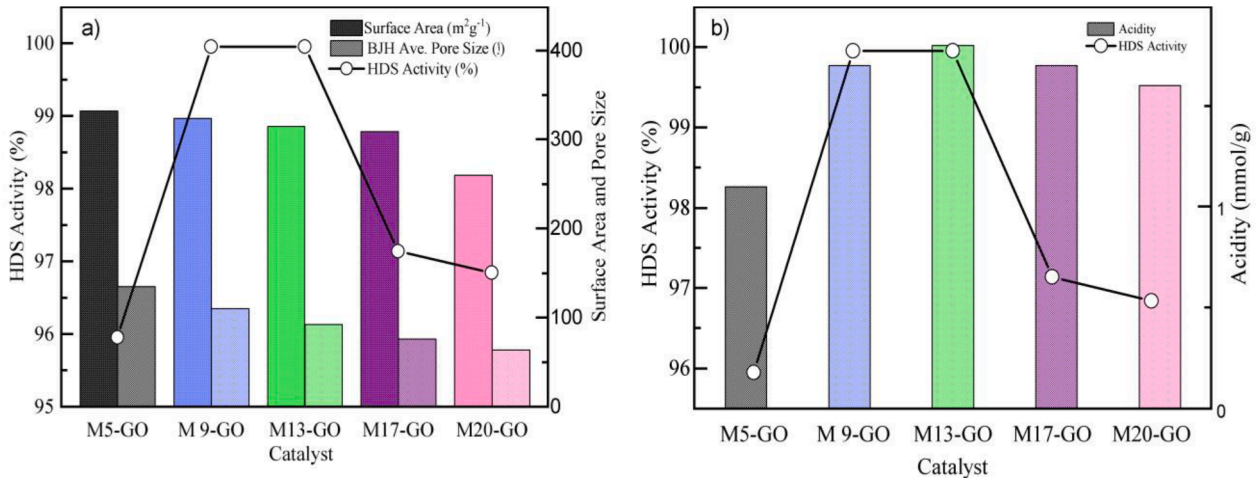

Fig. 8. The HDS conversion of MoS_2-GO nanocomposites catalysts as a function of a) the surface area, and the pore size as measured by N_2 adsorption–description, b) The acidity as measured by NH_3-TPD.

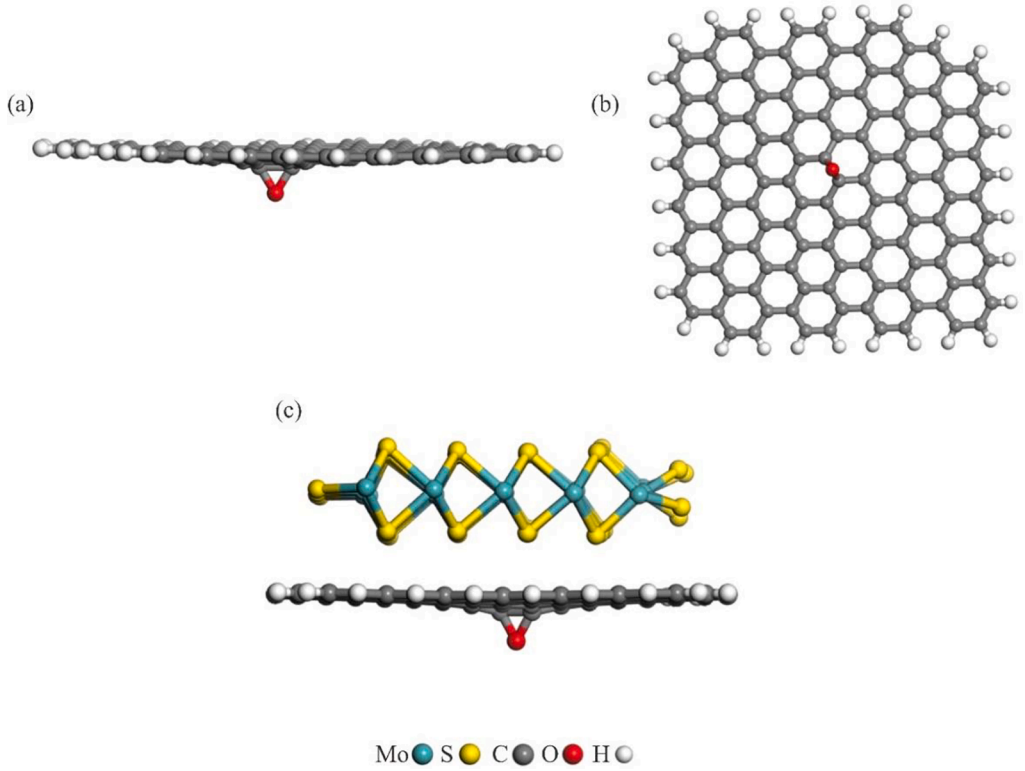

Fig. 9. (a) and (b) the molecular model of GO used in the present study (from two different views), and (c) the most stable geometry of MoS_2-GO.

be favorably dissociated on MoS_2 with 50% sulfur coverage at each edge. Hence, a 5 × 5 cluster of MoS_2 with 50% coverage of S atoms at each edge was decorated on the GO to construct MoS_2-GO. Fig. 9c shows the most stable structure of MoS_2-GO.The shortest distance between the MoS_2 and carbon atoms of GO in MoS_2-GO is 3.3 Å, which is in a good agreement with those values reported in previous studies [79]. Also, the adsorption energy of MoS_2 on the GO was calculated to be −12.5 kcal/mol indicating that the formed MoS_2-GO complex is thermodynamically stable at normal condition.

Now let us consider the adsorption of a single H_2 or DBT molecule over the MoS_2/GO. To find the most stable adsorption configuration of these species, many possible adsorption sites of the MoS_2/GO were checked, including Mo and S atoms or Mo-Mo, Mo-S and S-S bridges. Fig. 10 shows the optimized absorption forms of DBT and H_2 on the MoS_2-GO. For DBT molecule, two stable adsorption configurations were identified at the edges of MoS_2 (i.e., brim and sigma). Both these configurations were found to be stable due to the corresponding negative adsorption energies. However, our DFT calculations reveal that the adsorption of DBT on the brim of Mo- or S-edges of MoS_2 has a larger adsorption energy than that of sigma configuration (Fig. 10). Note also that the calculated E_{ads} values for the DBT in the present study are in good agreement with those reported by Sharifvaghefi et al. [67]. Associated with the adsorption of DBT, a considerable electronic charge (≈ 0.20 e) is transferred from the MoS_2 layer into DBT. These results clearly show the activation of DBT on the MoS_2-GO. On the other hand, H_2 molecule is found to be adsorbed at the edges of MoS_2 through a brim configuration (Fig. 10e and 10f). Unlike the Mo-edge, the physisorption of H_2 on the S-edge is exothermic due to the negative adsorption energy

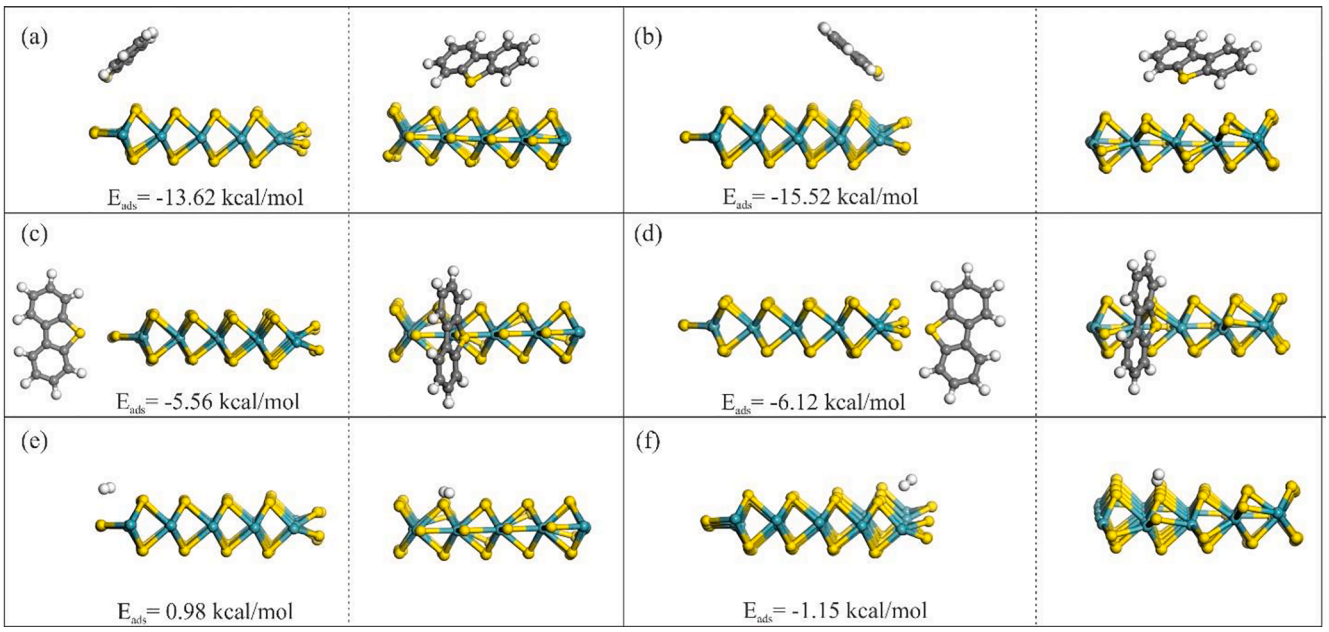

Fig. 10. The optimized adsorption configurations (from two different views) and adsorption energies (E_{ads}) of DBT and H_2 molecules on the MoS_2-GO. (a) DBT adsorption on the brim of Mo-edge, (b) DBT adsorption on the brim of S-edge, (c) sigma adsorption configuration of DBT at the Mo-edge, (d) sigma adsorption configuration of DBT at the S-edge, (e) H_2 adsorption on the brim of Mo-edge and (f) H_2 adsorption on the brim of S.-edge. The GO substrate is not shown for the simplicity.

of −1.15 kcal/ mol. Moreover, the Hirshfeld atomic charge analysis indicated that the adsorption of H_2 led to shift of 0.08 e from MoS_2 into H_2. We also examined the dissociation of adsorbed H_2 molecule to examine the stability of Mo-H or S-H bonds on the MoS_2-GO catalyst (Fig. 11). Similar to those previous studies [80–82], it is seen that the dissociation of H_2 is site-selective, and it requires a relatively larger activation energy at the Mo-edge than the S-edge. In particular, the activation energies needed for dissociation of H_2 on the Mo-edge than the S-edge are calculated to be 21.80 and 12.62 kcal/mol, respectively, which agree well with the reported values by Paul and Payen [80]. We note that other possible dissociative configurations of the H_2 molecule which include the formation of two S-H or two Mo-H groups were also investigated. Our results indicated that the formation of S-H and Mo-H bonds resulting from the dissociation of H_2 molecule is more energetically favorable than the formation of two Mo-H or S-H groups at both edges. Importantly, the less stability of two S-H bonds on the edges of MoS_2 suggests that the direct formation of SH_2 group should be inhibited at normal condition. Unlike the Mo-edge, the formation of S-H and Mo-H bonds on the S-edge is exothermic with an energy release of −4.24 kcal/ mol (see Fig. 11). These findings are consistent with those mentioned in Ref. 80, suggesting that the H_2 dissociation on the S-edge of MoS_2 is more favorable than the Mo-edge from both thermodynamic and kinetic points of view.

To shed light on the catalytic activity of MoS_2-GO, we examined the mono-hydrogenated DBT intermediates derived from the HDS reaction (HYD) and direct desulfurization (DDS) routes (Fig. 12a). For both routes, we only considered the brim sites of the MoS_2 since DBT molecule has a stronger interaction with them. Also, these hydrogenation reactions are driven by the highly reactive H atom of the adjacent S–H group on the pre-hydrogenated MoS_2. Fig. 12b shows the optimized structures of initial and final states involved in these mechanisms along with the corresponding formation energies (E_{form}). At the Mo-edge, one

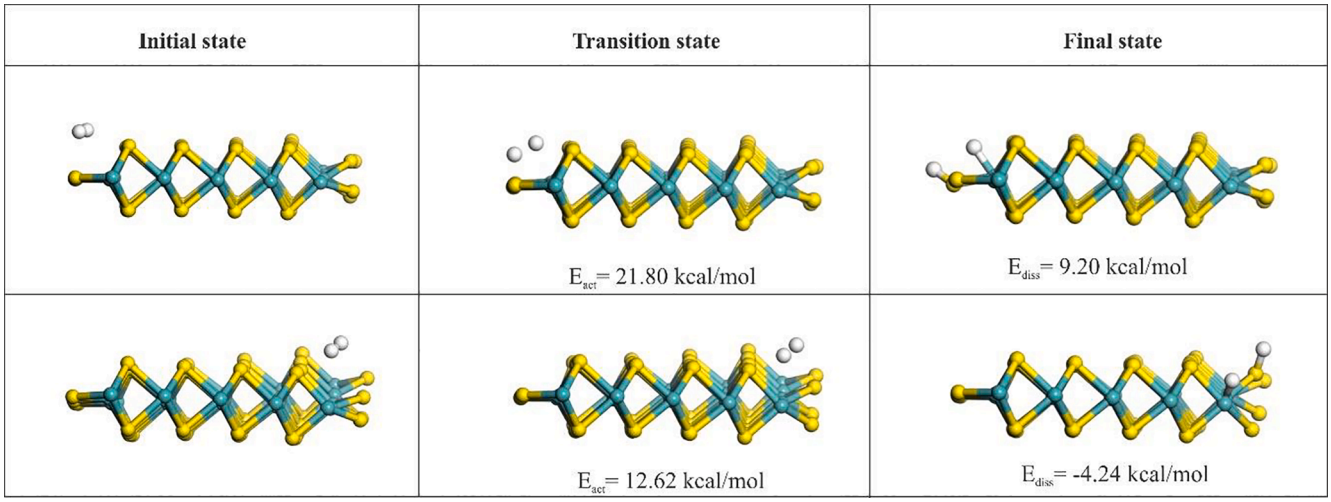

Fig. 11. The optimized geometries, activation energies and dissociation energies of H_2 at (a) Mo-, and (b) S-edge of MoS_2. The GO substrate is not shown for the simplicity.

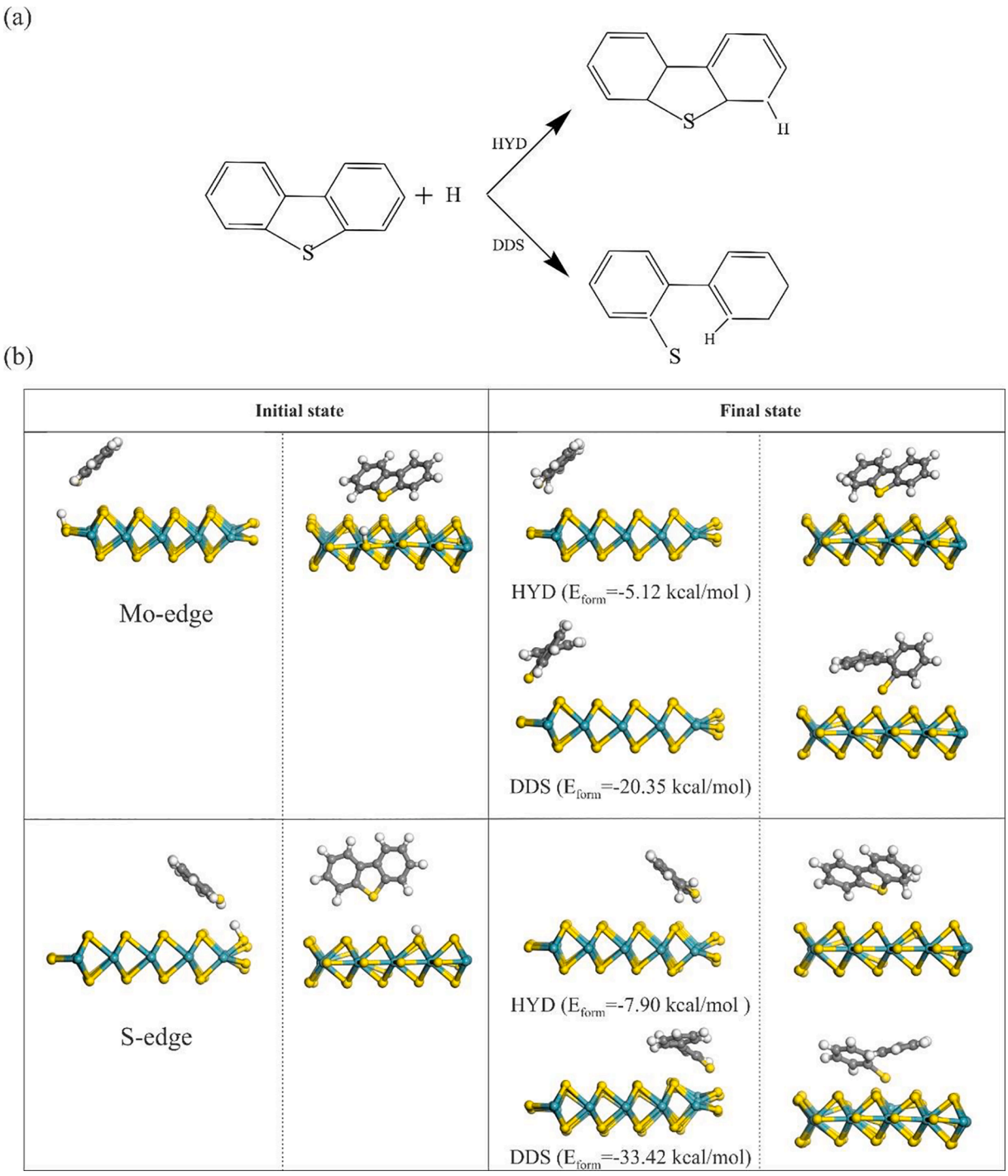

Fig. 12. (a) Possible routes for the hydrogenation of DBT, and (b) the optimized initial/final states and formation energies (E_{form}) for the HDS of DBT via the HYD and DDS routes. The E_{form} defines as $E_{form} = E_{final\ state}$-$E_{initial\ state}$. In (b) the GO substrate is not shown for the simplicity.

can see that the DDS process of DBT results in a more stable hydrogenated intermediate than HYD. This is verified by the calculated larger negative formation energy (E_{form}) of the former process. Considering the low dissociation energy of H_2 on this edge, these results clearly indicate that the Mo edge of MoS_2 is an active site for desulfurization of DBT. Also note that the hydrogenation of DBT via the HYD pathway has a negative E_{form} value, suggesting the possible formation of the corresponding hydrogenated species.

At the S-edge, it is also found that the E_{form} values of the DBT hydrogenation via both HYD and DDS pathways are negative (Fig. 12b). Similarly, our data reveal that the DDS route of DBT molecule leads to the formation of a more stable hydrogenated intermediate than HYD. However, for a given hydrogenation pathway, the formation energy associated with the S- edge of MoS_2 is more negative than that of Mo-edge. Consequently, the S-edge should have a larger ability to S-C bond scission of DBT. These findings are consistent with earlier experimental and theoretical results [81,83,84] ,suggesting that in the presence of vacancies, the DDS of DBT is more energetically favorable than HYD. This observation can be explained by a sizable charge transfer from MoS_2 surface into the adsorbed DBT molecule, which is much important on the S-edge than Mo-edge.

4. Conclusions

This study focused on a novel, low-cost, simplistic, high yield, and scalable method to prepare highly porous M−GO nanocomposites by reacting graphene oxide and co-exfoliation of commercial MoS_2 in the presence of the PVP under ultrasonication. When the ultrasonic output power is set to 80 W, the MoS_2 particle size is the smallest with an increase in specific surface area

and the pore volume. Accordingly, it helps the active metal be dispersed uniformly on GO and the formation of the more active sites which can be exposed to the HDS reaction. In addition, catalytic activities of the M−GO nanocomposite catalysts were investigated under a variety of operating conditions. Based on the results, the catalytic performance showed a trend of M9-GO ~ M13-GO≫Co-Mo/γAl_2O_3 > M17-GO > M20-GO > M5-GO at the operation condition (380 °C, 45 bars, LHSV: 0.8 h^{-1} and H_2/oil: 600NL.L^{-1}). Examination of physicochemical and chemical properties of the M−GO nanocomposites revealed that M9-GO with the excellent characteristics i.e., a higher levels of total acidity, high surface area (324 m^2g^{-1}) and large pore size (110.3 Å), low lateral size, increased porosity, and high dispersibility of the MoS_2 on GO sheets), resulted in the highest HDS performance, and reduced 16,800 ppm (1.68 wt%) sulfur of VGO feedstock to a sub10 ppm, which means a HDS efficiency about 99.95% compared to the Co-Mo/γAl_2O_3 as a commercial catalyst (350 ppm sulfur or 97.91% HDS efficiency) in similar operation condition. This considerable improvement is economically valuable. In addition, DFT calculations clarified that the H_2 dissociation is needs an activation energy of 21.80 and 12.62 kcal/mol, respectively, on the Mo- and S-edge of decorated MoS_2 clusters on the GO with 50% coverage. It was also found that the HDS of DBT molecule could take place at the edges of MoS_2 through a DDS pathway.

CRediT authorship contribution statement

Zohal Safaei Mahmoudabadi: Methodology, Data curation, Writing - original draft, Investigation. **Alimorad Rashidi:** Conceptualization, Methodology, Supervision, Writing - review & editing. **Ahmad Tavasoli:** Visualization, Supervision. **Mehdi Esrafili:** Software, Validation. **Mohammad Panahi:** Software, Data curation, Validation. **Mojtaba Askarieh:** Visualization, Writing - review & editing. **Saeed Khodabakhshi:** Visualization, Writing - review & editing.

Declaration of Competing Interest

The authors declare that they have no known competing financial interests or personal relationships that could have appeared to influence the work reported in this paper.

Appendix A. Supplementary data

Supplementary data to this article can be found online at https://doi.org/10.1016/j.ultsonch.2021.105558.

References

[1] P. Grange, Catalytic hydrodesulfurization, Catal. Rev. Eng. 21 (1) (1980) 135–181.

[2] Y. Ding, Y. Zhou, W. Nie, P. Chen, MoS_2 -GO nanocomposites synthesized via a hydrothermal hydrogel method for solar light photocatalytic degradation of methylene blue, Appl. Surf. Sci. 357 (2015) 1606–1612, https://doi.org/10.1016/j.apsusc.2015.10.030.

[3] G. Li, Y. Li, G. Lin, D.a. Wang, P. Guo, X. Li, K.H. Chung, Synthesis of unsupported Co-Mo hydrodesulfurization catalysts with ethanol-water mixed solvent: Effects of the ethanol/water ratio on active phase composition, morphology and activity, Appl. Catal. A Gen. 602 (2020) 117663, https://doi.org/10.1016/j.apcata.2020.117663.

[4] I. Ali, T.A. Saleh, Zeolite-Graphene composite as support for Molybdenum-based catalysts and their Hydrodesulfurization performance, Appl. Catal. A Gen. 598 (2020) 117542, https://doi.org/10.1016/j.apcata.2020.117542.

[5] P.S. Sinhmar, P.R. Gogate, Ultrasound assisted oxidative deep-desulfurization of dimethyl disulphide from turpentine, Ultrason. Sonochem. 63 (2020) 104925, https://doi.org/10.1016/j.ultsonch.2019.104925.

[6] N.S. More, P.R. Gogate, Intensified desulfurization of simulated crude diesel containing thiophene using ultrasound and ultraviolet irradiation, Ultrason. Sonochem. 58 (2019) 104612, https://doi.org/10.1016/j.ultsonch.2019.104612.

[7] Y. Lin, L.i. Feng, X. Li, Y. Chen, G. Yin, W. Zhou, Study on ultrasound-assisted oxidative desulfurization for crude oil, Ultrason. Sonochem. 63 (2020) 104946, https://doi.org/10.1016/j.ultsonch.2019.104946.

[8] Z.S. Mahmoudabadi, A. Rashidi, A. Tavasoli, Synthesis of MoS_2 quantum dots as a nanocatalyst for hydrodesulfurization of Naphtha: Experimental and DFT study, J. Environ. Chem. Eng. 8 (3) (2020) 103736, https://doi.org/10.1016/j.jece:2020.103736.

[9] Z.S. Mahmoudabadi, A. Tavasoli, A. Rashidi, M. Esrafili, Catalytic activity of synthesized 2D MoS_2/graphene nanohybrids for the hydrodesulfurization of SRLGO: experimental and DFT study, Environ. Sci. Pollut. Res. 28 (5) (2021) 5978–5990.

[10] Z. Safaei Mahmoudabadi, A. Rashidi, M. Panahi, New approach to unsupported ReS_2 nanorod catalyst for upgrading of heavy crude oil using methane as hydrogen source, Int. J. Hydrogen Energy. 46 (7) (2021) 5270–5285.

[11] T.A. Saleh, S.A. AL-Hammadi,, A novel catalyst of nickel-loaded graphene decorated on molybdenum-alumina for the HDS of liquid fuels, Chem. Eng. J. 406 (2021), 125167.

[12] G.M.K. Abotsi, A.W. Scaroni, A Review of Carbon-Supported Hydrodesulfurization, Catalysts 22 (1989) 107–133.

[13] D. Gao, A. Duan, X. Zhang, Z. Zhao, E. Hong, J. Li, H. Wang, Applied Catalysis B : Environmental Synthesis of NiMo catalysts supported on mesoporous Al-SBA-15 with different morphologies and their catalytic performance of DBT HDS, "Applied Catal, B, Environ. 165 (2015) 269–284, https://doi.org/10.1016/j.apcatb.2014.10.034.

[14] C. Peng, R. Guo, X. Feng, X. Fang, Tailoring the structure of Co-Mo/mesoporous γ-Al_2O_3 catalysts by adding multi-hydroxyl compound: A 3000 kt/a industrial-scale diesel ultra-deep hydrodesulfurization study, Chem. Eng. J. 377 (2019) 119706, https://doi.org/10.1016/j.cej.2018.08.092.

[15] C. Guo, T. Zhang, M. Niu, S. Cao, S. Wei, Z. Wang, W. Guo, X. Lu, C.M.L. Wu, Impact of diverse active sites on MoS_2 catalyst: Competition on active site formation and selectivity of thiophene hydrodesulfurization reaction, Mol. Catal. 463 (2019) 67–76, https://doi.org/10.1016/j.mcat.2018.11.014.

[16] H. Schweiger, P. Raybaud, G. Kresse, H. Toulhoat, Shape and edge sites modifications of MoS_2 catalytic nanoparticles induced by working conditions: A theoretical study, J. Catal. 207 (1) (2002) 76–87, https://doi.org/10.1006/jcat.2002.3508.

[17] S. Eijsbouts, J.J.L. Heinerman, H.J.W. Elzerman, MoS_2 structures in high-activity hydrotreating catalysts. I. Semi-quantitative method for evaluation of transmission electron microscopy results. Correlations between hydrodesulfurization and hydrodenitrogenation activities and MoS_2 dispersion, Appl. Catal. A, Gen. 105 (1) (1993) 53–68, https://doi.org/10.1016/0926-860X(93)85133-A.

[18] J.L. García-Gutiérrez, G.C. Laredo, G.A. Fuentes, P. García-Gutiérrez, F. Jiménez-Cruz, Effect of nitrogen compounds in the hydrodesulfurization of straight-run gas oil using a CoMoP/g-Al2O3 catalyst, Fuel. 138 (2014) 98–103.

[19] C.T. Tye, K.J. Smith, Hydrodesulfurization of dibenzothiophene over exfoliated MoS_2 catalyst, Catal. Today. 116 (4) (2006) 461–468, https://doi.org/10.1016/j.cattod.2006.06.028.

[20] M. Daage, R.R. Chianelli, Structure-function relations in molybdenum sulfide catalysts: the" rim-edge" model, J. Catal. 149 (1994) 414–427.

[21] H. Farag, K. Sakanishi, M. Kouzu, A. Matsumura, Y. Sugimoto, I. Saito, Dibenzothiophene hydrodesulfurization over synthesized MoS_2 catalysts, J. Mol. Catal. A Chem. 206 (1-2) (2003) 399–408, https://doi.org/10.1016/S1381-1169(03)00445-X.

[22] J.L. García-gutiérrez, G.C. Laredo, G.A. Fuentes, P. García-gutiérrez, F. Jiménez-cruz, Effect of nitrogen compounds in the hydrodesulfurization of straight-run gas oil using a CoMoP / g-Al2O3 catalyst, (2014) 2–7. https://doi.org/10.1016/j.fuel.2014.08.008.

[23] H. Zhang, H. Lin, Y. Zheng, Application of Uniform Design Method in the Optimization of Hydrothermal Synthesis for Nano MoS_2 Catalyst with High HDS Activity, Catalysts. 8 (2018) 654.

[24] A. Cho, S.H. Moon, Development of highly active Co(Ni)Mo catalysts for the hydrodesulfurization of dibenzothiophene compounds, Catal. Surv. from Asia. 14 (2) (2010) 64–74, https://doi.org/10.1007/s10563-010-9088-2.

[25] I. Vázquez-Garrido, A. López-Benítez, G. Berhault, A. Guevara-Lara, Effect of support on the acidity of NiMo/Al_2O_3-MgO and NiMo/TiO_2-Al_2O_3 catalysts and on the resulting competitive hydrodesulfurization/hydrodenitrogenation reactions, Fuel. 236 (2019) 55–64.

[26] I. Ali, A.A. Al-Arfaj, T.A. Saleh, Carbon nanofiber-doped zeolite as support for molybdenum based catalysts for enhanced hydrodesulfurization of dibenzothiophene, J. Mol. Liq. 304 (2020), 112376.

[27] Y. Li, W. Gao, L. Ci, C. Wang, P.M. Ajayan, Catalytic performance of Pt nanoparticles on reduced graphene oxide for methanol electro-oxidation, Carbon N. Y. 48 (4) (2010) 1124–1130.

[28] J.Y. Jhan, Y.W. Huang, C.H. Hsu, H. Teng, D. Kuo, P.L. Kuo, Three-dimensional network of graphene grown with carbon nanotubes as carbon support for fuel cells, Energy. 53 (2013) 282–287, https://doi.org/10.1016/j.energy.2013.03.002.

[29] W. Xu, X. Wang, Q. Zhou, B. Meng, J. Zhao, J. Qiu, Y. Gogotsi, Low-temperature plasma-assisted preparation of graphene supported palladium nanoparticles with high hydrodesulfurization activity, J. Mater. Chem. 22 (2012) 14363–14368, https://doi.org/10.1039/c2jm16479e.

[30] Z. Hajjar, M. Kazemeini, A. Rashidi, S. Soltanali, Optimizing parameters affecting synthesis of a novel Co–Mo/GO catalyst in a Naphtha HDS reaction utilizing D-optimal experimental design method, J. Taiwan Inst. Chem. Eng. 78 (2017) 566–575, https://doi.org/10.1016/j.jtice.2017.06.048.

[31] N. Liu, X. Wang, W. Xu, H. Hu, J. Liang, J. Qiu, Microwave-assisted synthesis of MoS2/graphene nanocomposites for efficient hydrodesulfurization, Fuel. 119 (2014) 163–169, https://doi.org/10.1016/j.fuel.2013.11.045.

[32] Z.S. Mahmoudabadi, A. Rashidi, A. Tavasoli, M. Bazmi, H. Farshidi, Oxidative desulfurization of liquid fuels using metal sulfide quantum dots/graphen oxid hybrid nanocatalyst, (2020).

[33] R. Ambati, P.R. Gogate, Ultrasound assisted synthesis of iron doped TiO_2 catalyst, Ultrason. Sonochem. 40 (2018) 91–100, https://doi.org/10.1016/j.ultsonch.2017.07.002.

[34] A. Amiri, P. Sharifian, N. Soltanizadeh, Application of ultrasound treatment for improving the physicochemical, functional and rheological properties of myofibrillar proteins, Int. J. Biol. Macromol. 111 (2018) 139–147, https://doi.org/10.1016/j.ijbiomac.2017.12.167.

[35] L. shi, B. Duan, Z. Zhu, C. Sun, J. Zhou, A. Walsh, Preparing copper catalyst by ultrasound-assisted chemical precipitation method, Ultrason. Sonochem. 64 (2020) 105013, https://doi.org/10.1016/j.ultsonch.2020.105013.

[36] Z. Wang, R. Fang, H. Guo, Advances in ultrasonic production units for enhanced oil recovery in China, Ultrason. Sonochem. 60 (2020), 104791.

[37] L. Shi, Z. Zhang, R. Wang, C. Zhou, C. Sun, Study on ultrasound-assisted precipitation for preparing Ni/Al_2O_3 catalyst, Ultrason. Sonochem. 67 (2020) 105107, https://doi.org/10.1016/j.ultsonch.2020.105107.

[38] R. Kronberg, M. Hakala, N. Holmberg, K. Laasonen, Hydrogen adsorption on MoS_2-surfaces: A DFT study on preferential sites and the effect of sulfur and hydrogen coverage, Phys. Chem. Chem. Phys. 19 (24) (2017) 16231–16241, https://doi.org/10.1039/C7CP03068A.

[39] S. Posysaev, M. Alatalo, Surface Morphology and Sulfur Reduction Pathways of MoS_2 Mo Edges of the Monolayer and (100) and (103) Surfaces by Molecular Hydrogen: A DFT Study, ACS Omega. 4 (2) (2019) 4023–4028, https://doi.org/10.1021/acsomega.8b0299010.1021/acsomega.8b02990.s001.

[40] P. Zheng, T. Li, K. Chi, C. Xiao, J. Fan, X. Wang, A. Duan, DFT insights into the formation of sulfur vacancies over corner/edge site of Co/Ni-promoted MoS_2 and WS_2 under the hydrodesulfurization conditions, Appl. Catal. B Environ. 257 (2019) 117937, https://doi.org/10.1016/j.apcatb.2019.117937.

[41] S. William, J.R. Hummers, R.E. Offeman, Preparation of graphitic oxide, J. Am. Chem. Soc. 80 (1958) 1339.

[42] J. Chen, Y. Li, L. Huang, C. Li, G. Shi, High-yield preparation of graphene oxide from small graphite flakes via an improved Hummers method with a simple purification process, Carbon N. Y. 81 (2015) 826–834.

[43] B. Delley, An all-electron numerical method for solving the local density functional for polyatomic molecules, J. Chem. Phys. 92 (1) (1990) 508–517, https://doi.org/10.1063/1.458452.

[44] J.P. Perdew, K. Burke, M. Ernzerhof, Generalized gradient approximation made simple, Phys. Rev. Lett. 77 (18) (1996) 3865–3868, https://doi.org/10.1103/PhysRevLett.77.3865.

[45] S. Grimme, Accurate description of van der Waals complexes by density functional theory including empirical corrections, J. Comput. Chem. 25 (12) (2004) 1463–1473, https://doi.org/10.1002/(ISSN)1096-987X10.1002/jcc.v25:1210.1002/jcc.20078.

[46] B. Delley, Hardness conserving semilocal pseudopotentials, Phys. Rev. B - Condens. Matter Mater. Phys. 66 (2002) 1–9, https://doi.org/10.1103/PhysRevB.66.155125.

[47] N. Govind, M. Petersen, G. Fitzgerald, D. King-Smith, J. Andzelm, A generalized synchronous transit method for transition state location 28 (2) (2003) 250–258, https://doi.org/10.1016/S0927-0256(03)00111-3.

[48] C.M. Koo, H.T. Ham, M.H. Choi, S.O. Kim, I.J. Chung, Characteristics of polyvinylpyrrolidone-layered silicate nanocomposites prepared by attrition ball milling, Polymer (Guildf). 44 (3) (2003) 681–689, https://doi.org/10.1016/S0032-3861(02)00803-0.

[49] A.B. Bourlinos, V. Georgakilas, R. Zboril, T.A. Steriotis, A.K. Stubos, C. Trapalis, Aqueous-phase exfoliation of graphite in the presence of polyvinylpyrrolidone for the production of water-soluble graphenes, Solid State Commun. 149 (47-48) (2009) 2172–2176, https://doi.org/10.1016/j.ssc.2009.09.018.

[50] A. Stanislaus, A. Marafi, M.S. Rana, Recent advances in the science and technology of ultra low sulfur diesel (ULSD) production, 153 (2010) 1–68. https://doi.org/10.1016/j.cattod.2010.05.011.

[51] J.H. Robertson, Elements of X-ray diffraction by, BD Cullity (1979).

[52] Z. Hajjar, M. Kazemeini, A. Rashidi, M. Bazmi, In Situ and Simultaneous Synthesis of a Novel Graphene-Based Catalyst for Deep Hydrodesulfurization of Naphtha, Catal. Letters. 145 (9) (2015) 1660–1672, https://doi.org/10.1007/s10562-015-1563-y.

[53] D. Kong, H. Wang, J.J. Cha, M. Pasta, K.J. Koski, J. Yao, Y. Cui, Synthesis of MoS2 and MoSe2 films with vertically aligned layers, Nano Lett. 13 (3) (2013) 1341–1347, https://doi.org/10.1021/nl400258t.

[54] F. Yin, S. Wu, Y. Wang, L. Wu, P. Yuan, X. Wang, Self-assembly of mildly reduced graphene oxide monolayer for enhanced Raman scattering, J. Solid State Chem. 237 (2016) 57–63, https://doi.org/10.1016/j.jssc.2016.01.015.

[55] J. Chen, B. Yao, C. Li, G. Shi, An improved Hummers method for eco-friendly synthesis of graphene oxide, Carbon N. Y. 64 (2013) 225–229.

[56] L. Yang, X.-zhen. Wang, Y. Liu, Z.-fa. Yu, J.-jing. Liang, B.-bing. Chen, C. Shi, S. Tian, X. Li, J.-shan. Qiu, Monolayer MoS2 anchored on reduced graphene oxide nanosheets for efficient hydrodesulfurization, Appl. Catal. B Environ. 200 (2017) 211–221, https://doi.org/10.1016/j.apcatb.2016.07.006.

[57] O. Akhavan, The effect of heat treatment on formation of graphene thin films from graphene oxide nanosheets, Carbon N. Y. 48 (2) (2010) 509–519, https://doi.org/10.1016/j.carbon.2009.09.069.

[58] A. Nourmohammadi, R. Rahighi, O. Akhavan, A. Moshfegh, Graphene oxide sheets involved in vertically aligned zinc oxide nanowires for visible light photoinactivation of bacteria, J. Alloys Compd. 612 (2014) 380–385, https://doi.org/10.1016/j.jallcom.2014.05.195.

[59] Y. Li, H. Wang, L. Xie, Y. Liang, G. Hong, H. Dai, MoS2 nanoparticles grown on graphene: an advanced catalyst for the hydrogen evolution reaction, J. Am. Chem. Soc. 133 (2011) 7296–7299.

[60] J.A.R. van Veen, H.A. Colijn, P.A.J.M. Hendriks, A.J. van Welsenes, On the formation of type I and type II NiMoS phases in $NiMo/Al_2O_3$ hydrotreating catalysts and its catalytic implications, Fuel Process. Technol. 35 (1-2) (1993) 137–157, https://doi.org/10.1016/0378-3820(93)90089-M.

[61] M.A. Al-Daous, Graphene-MoS2 composite: Hydrothermal synthesis and catalytic property in hydrodesulfurization of dibenzothiophene, Catal. Commun. 72 (2015) 180–184, https://doi.org/10.1016/j.catcom.2015.09.030.

[62] P. Afanasiev, The influence of reducing and sulfiding conditions on the properties of unsupported MoS_2-based catalysts, J. Catal. 269 (2) (2010) 269–280, https://doi.org/10.1016/j.jcat.2009.11.004.

[63] R.L. AL Otaibi, D. Liu, X. Hou, L. Song, Q. Li, M. Li, H.O. Almigrin, Z. Yan, Desulfurization of Saudi Arabian crudes by oxidation – extraction method, Appl. Petrochemical Res. 5 (4) (2015) 355–362, https://doi.org/10.1007/s13203-015-0112-3.

[64] A. Parulkar, J.A. Thompson, M. Hurt, B.-Z. Zhan, N.A. Brunelli, Improving Hydrodenitrogenation Catalyst Performance through Analyzing Hydrotreated Vacuum Gas Oil Using Ion Mobility-Mass Spectrometry, Ind. Eng. Chem. Res. 57 (27) (2018) 8845–8854, https://doi.org/10.1021/acs.iecr.8b0103810.1021/acs.iecr.8b01038.s001.

[65] F.C.-Y. Wang, W.K. Robbins, F.P. Di Sanzo, F.C. McElroy, Speciation of sulfur-containing compounds in diesel by comprehensive two-dimensional gas chromatography, J. Chromatogr. Sci. 41 (2003) 519–523.

[66] X. Ma, K. Sakanishi, I. Mochida, Hydrodesulfurization reactivities of various sulfur compounds in vacuum gas oil, Ind. Eng. Chem. Res. 35 (8) (1996) 2487–2494.

[67] S. Sharifvaghefi, B. Yang, Y. Zheng, New insights on the role of H_2S and sulfur vacancies on dibenzothiophene hydrodesulfurization over MoS2 edges, Appl. Catal. A Gen. 566 (2018) 164–173.

[68] Q. Jin, B. Chen, Z. Ren, X. Liang, N. Liu, D. Mei, A theoretical study on reaction mechanisms and kinetics of thiophene hydrodesulfurization over MoS_2 catalysts, Catal. Today. 312 (2018) 158–167.

[69] D. Valencia, T. Klimova, Citric acid loading for MoS_2-based catalysts supported on SBA-15. New catalytic materials with high hydrogenolysis ability in hydrodesulfurization, Appl. Catal. B Environ. 129 (2013) 137–145.

[70] S.P. Lonkar, V. Pillai, S.M. Alhassan, J. Accepted, Three Dimensional Heterostructured Nanohybrids as High-performance Hydrodesulfurization Catalysts (2018), https://doi.org/10.1021/acsanm.8b00287.

[71] A.N. Varakin, A. V Mozhaev, A.A. Pimerzin, P.A. Nikulshin, SC, "Applied Catal. B, Environ. (2018). https://doi.org/10.1016/j.apcatb.2018.04.003.

[72] S.P. Lonkar, V.V. Pillai, S.M. Alhassan, Three-Dimensional NiS-MoS_2/Graphene Heterostructured Nanohybrids as High-Performance Hydrodesulfurization Catalysts, ACS Appl. Nano Mater. 1 (7) (2018) 3114–3123, https://doi.org/10.1021/acsanm.8b0028710.1021/acsanm.8b00287.s001.

[73] M. Salimi, A. Tavasoli, S. Balou, H. Hashemi, K. Kohansal, SC, "Applied Catal. B, Environ. (2018). https://doi.org/10.1016/j.apcatb.2018.08.039.

[74] F. Hasanpour, J. Saien, Incorporating Pb2 + Templates into the Crystalline Structure of MnO2 Catalyst Supported on Monolith : Applications in H2O2 Decomposition, (2019). https://doi.org/10.1021/acsomega.9b02565.

[75] M.F. Abid, S.M. Ahmed, W.H. Abohameed, S.M. Ali, Study on Hydrodesulfurization of a Mixture of Middle Distillates, Arab. J. Sci. Eng. 43 (11) (2018) 5837–5850, https://doi.org/10.1007/s13369-017-3005-1.

[76] P.G. Moses, B. Hinnemann, H. Topsøe, J.K. Nørskov, The hydrogenation and direct desulfurization reaction pathway in thiophene hydrodesulfurization over MoS_2 catalysts at realistic conditions: A density functional study, J. Catal. 248 (2007) 188–203.

[77] P.G. Moses, B. Hinnemann, H. Topsøe, J.K. Nørskov, The effect of Co-promotion on MoS_2 catalysts for hydrodesulfurization of thiophene: A density functional study, J. Catal. 268 (2009) 201–208.

[78] P. Zheng, T. Li, K. Chi, C. Xiao, J. Fan, X. Wang, A. Duan, DFT insights into the formation of sulfur vacancies over corner/edge site of Co/Ni-promoted MoS_2 and WS_2 under the hydrodesulfurization conditions, Appl. Catal. B Environ. 257 (2019), 117937.

[79] D. Sun, D. Ye, P. Liu, Y. Tang, J. Guo, L. Wang, H. Wang, MoS_2/Graphene nanosheets from commercial bulky MoS_2 and graphite as anode materials for high rate sodium-Ion batteries, Adv. Energy Mater. 8 (2018) 1702383.

[80] J. Paul, E. Payen, Vacancy formation on MoS_2 hydrodesulfurization catalyst: DFT study of the mechanism, J. Phys. Chem. B 107 (2003) 4057–4064.

[81] S. Ding, S. Jiang, Y. Zhou, Q. Wei, W. Zhou, Catalytic characteristics of active corner sites in CoMoS nanostructure hydrodesulfurization–A mechanism study based on DFT calculations, J. Catal. 345 (2017) 24–38.

[82] J.V. Lauritsen, M. Nyberg, J.K. Nørskov, B.S. Clausen, H. Topsøe, E. Lægsgaard, F. Besenbacher, Hydrodesulfurization reaction pathways on MoS_2 nanoclusters revealed by scanning tunneling microscopy, J. Catal. 224 (1) (2004) 94–106.
[83] P.-Y. Prodhomme, P. Raybaud, H. Toulhoat, Free-energy profiles along reduction pathways of MoS_2 M-edge and S-edge by dihydrogen: A first-principles study, J. Catal. 280 (2011) 178–195.
[84] J. Chen, F. Maugé, J. El Fallah, L. Oliviero, IR spectroscopy evidence of MoS_2 morphology change by citric acid addition on MoS_2/Al_2O_3 catalysts–A step forward to differentiate the reactivity of M-edge and S-edge, J. Catal. 320 (2014) 170–179.